Non-destructive evaluation of isotropic plate structures by means of mode filtering in the frequency-wavenumber domain

Frederick A.F. Purcell[a,*], Mark Eaton[a], Matthew Pearson[a], Rhys Pullin[a]

[a] *Cardiff School of Engineering, Cardiff University, Cardiff, CF24 3AA, UK*

Abstract

Non-Destructive Testing (NDT) techniques are prevalent in the aerospace, green energy and automotive industries. These techniques, including ultrasound, despite their use, still have limitations surrounding speed and resolution. This work presents the development of a band-pass mode filtering technique in the frequency wavenumber domain for the purpose of damage detection in isotropic materials. Data was captured in the temporal and spatial domain using a 3D Scanning Laser Doppler Vibrometer (SLDV) with piezoelectric transducers exciting the structure with a variety of steady state signals ranging in frequency from 75kHz to 400kHz and a frequency modulated signal from 75kHz to 400kHz. A thickness map was created based on the frequency and wavelength of the A_0 Lamb wave mode. The technique was demonstrated on two aluminium specimens with dimensions of 400mm by 400mm with a thickness range of 0.5mm to 8mm with distinct geometric features. Through using multi-frequency excitation combined with mode based filters an estimation of thickness was achieved with a mean percentage thickness error of 15%. Circular thickness reductions with a diameter of 10mm were clearly identified at the maximum plate thickness of 8mm. This technique was shown to perform better than wavenumber filtering by allowing data from multi frequency steady state excitation to be combined into a single resulting thickness map. This improvement was shown to be particularly important at greater thicknesses.

Keywords: Wavenumber, spectroscopy, Lamb waves, Mode filtering, Damage detection, NDT

1. Introduction

From the aerospace to automotive industry the use of advanced materials as well as complex geometries is ever increasing with the drive to create lightweight structures. These structures require inspection once manufactured and then

*Corresponding author

periodically whilst in service. Due to the nature of these structures new demands are being placed on Non-Destructive Evaluation (NDE) techniques. In the aerospace industry the associated cost of inspection time can be very high, further driving the need to reduce inspection intervals by increasing the quality and accuracy of NDE techniques, as well as reducing the time and cost of carrying out inspections [1].

Thickness reductions can be key for identifying corrosion in metallics, as well as de-lamination and de-bonding defects in composite structures. Current techniques commonly used to identify and quantify these types of defects are based around contact ultrasound such as C-scan or A-scan. While these techniques are very reliable, robust and can offer good spatial and depth resolution, they can be slow since a probe has to be physically moved over the surface of the structure, which also causes probe wear. Furthermore challenging environments such as those found in the nuclear industry can often make contact methods impractical. Complications also arise when complex geometries are to be tested where custom or flexible probes are required to make good contact with the surface.

Other techniques have been proposed include thermal pulse NDT [2], air coupled ultrasound and Eddy current imaging [3] which all have various limitations. Guided wave ultrasound techniques have been proposed in many different configurations and have shown great promise [3]. A key feature of guided wave techniques being the ability to use low sensor densities. Widely used techniques such as visual inspection and tap testing further demonstrate the need for new techniques that can quickly and effectively quantify defects [4]. While these techniques offer the ability to locate damage in a region and give an index of damage, they have limited ability to quantify damage due to their limited data density.

Wavenumber, the spatial frequency, of a guided Lamb wave can be correlated to material thickness and properties, temporal frequency and wave mode. Analysis in the wavenumber domain has been proposed in a number of guided wave applications, for instance impact location [5, 6], crack detection [7] and delamination detection [8]. These techniques all make use of wavenumber as a key feature in defect detection and localization thereby gaining this spatial information with small transducer arrays.

Changes in wavenumber can be used to identify thickness changes [9]. Delamination defects in composite structures can be thought of as effective thickness changes in this context and as such defects such as corrosion and delamination are identifiable through a change in wavenumber. Wavenumber estimation for the purpose of defect and delamination detection has been proposed in a number of works [9, 10, 11, 12]. Despite differences in processing methods the concept relies on exciting guided Lamb waves in a structure, capturing full field wave data and extracting wavenumber information. Full field data can be captured by using a single fixed transducer to excite a guided wave and measuring spatial sampling points [9], or by exiting the structure at a number of spatial sample points and measuring the response at a single fixed point [13]. The full field data that is obtained, containing spacial and temporal information, is

analogous to a video of a wave passing though the structure.

Lamb waves will have a minimum of two modes present in plate-like structures, the fundamental anti-symmetric and symmetric modes denoted by A_0 and S_0 respectively. To obtain thickness estimation, only one mode can be present in the data, as the fundamental modes will have different wavenumbers at the same thickness-frequency product due to their dispersive nature. Much of the previous work relies on the fact that the A_0 mode is dominant in the out-of-plane motion [14]. This, combined with a measurement technique that only measures out-of-plane motion, such as a 1D Scanning Laser Doppler Vibrometer (LDV), can provide good estimations of thickness [9]. Other researchers have proposed the use of a bandpass mode filter to filter one mode out of the full wave-field data captured [11, 13, 12].

Two main classes of approach used to obtain wavenumber estimates are the Local Wavenumber Mapping (LWM) approach [10, 12, 15] or Acoustic Wavenumber Spectroscopy (AWS) as developed by Flynn [12, 13]. The LWM approach relies on a spatial window inside which the dominant wavenumber can be found using a 2D Fast Fourier Transform (FFT). An inherent problem with this approach is the trade-off between spatial and wavenumber resolution, which translates to depth resolution. Aspects of this can be mitigated by using overlapping windows [12, 16], but these issues will be exacerbated by any parts with greater thickness as the wavelength of Lamb waves increases. AWS passes the response through a bank of narrow band wavenumber filters and assigns each point the wavenumber of the filter which maximises the energy at that point [13]. Due to the relation between wavenumber, frequency and thickness, wavenumber values are only useful at a single frequency when trying to detect thickness changes. A single frequency may however not be suitable to excite an entire structure effectively. Multi-tone excitation has been proposed in conjunction with AWS [10]. This technique separated the response at different frequencies giving a wavenumber map at each frequency.

There are a number of methods available to acquire full field scan data with temporal and spatial information. Laser Doppler Vibrometer (LDV) uses the Doppler effect to identify the velocity of a surface from which a laser beam is reflected. This technique can be used to capture guided waves [17, 18, 19]. In a one dimensional set-up they are only able to capture the out-of-plane motion of the a plate at a single point. When combined with a galvanometer mirror system the single laser beam can be driven over an area of a structure giving it a scanning ability, making it a Scanning Laser Doppler Vibrometer (SLDV). The range is however limited as the angle of incidence of the laser to the test specimen can not be too great as the signal to noise ratio of out-of-plane displacement deteriorates as the angel of incidence increases. For a complex curved structure this measurement technique would therefore not be adequate. Other techniques such as air coupled ultrasound are also able to capture guided waves [17] but may not be practical in real world situations as the ultrasound probe is required to be placed a set distance over the structure surface making it difficult to use for complex geometries without complex automation. Pulsing laser ultrasound mitigates most of these problems but faces similar problems to a SLDV system

in that high incidence angles to the structure being excited will cause errors in the measurement. Furthermore the higher powered lasers required increased safety precautions as well as carrying potential to cause micro damage on the surface of the structure [20].

A Three Dimensional Scanning Laser Doppler Vibrometer (3D SLDV) can also be used to capture guided Lamb waves [21]. A 3D SLDV system consists of three SLDVs that are located at different angles to the sample. They have various benefits over SLDV or LDV systems, namely their ability to measure velocity in three dimensions on complex geometries and that the angle of incidence can be greater. Velocity data can then be calculated for in- and out-of-plane orientations. This is achievable as the three laser heads can be placed at different angles to the part allowing the displacement of a point to be triangulated. For this work a 3D SLDV was chosen for its ability to complete measurements on three dimensional parts in the future as well the high levels automation possible without detailed prior knowledge of the sample.

This work proposes the novel method of bandpass mode filtering to a calculated guided wave mode centred around a particular thickness in order to determine the most probable thickness at each measurement point. By finding the instantaneous amplitude post filtering to a given mode a thickness map can be found by assigning the thickness of the filter that maximises energy at each point. Unlike previous techniques this allows multi frequency excitation to be used and analysed with a single filter stack as the dispersive nature of Lamb waves is taken into account. The aim of the algorithm proposed is to use multi frequency excitation to achieve a greater data volume and attain low noise and accurate thickness maps even from parts with thickness ranges larger then 5mm, a current limitation.

2. Materials and methods

2.1. Full field data acquisition

The following sections describe the developed processing algorithm used to calculate a thickness estimate map from wave-field data using mode filtering. The process is the same for steady state or transient excitation as well as single or multi frequency excitation data. In order to present the steps of this algorithm it is demonstrated on an specimen, Phantom 1. For the example data a steady state excitation sine wave was used to excite a 3mm x 350mm x 350mm aluminium plate with three circular areas of 30mm diameter with reduced thickness of 1mm, 1.5mm and 2mm. The frequency of the driving sine wave was linearly modulated between 75 kHz and 400 kHz at a rate of 2.6 kHz. A Vallen System VS900-M transducer was driven at 200Vpp. The flat front face of Phantom 1 was scanned using a Polytec PSV-500-3D-M with 260 samples in each spatial axis covering an area of 300mm by 300mm. The maximum temporal sampling frequency of 2.56 MHz with 1024 sample length was used.

Figure 1 shows a flow chart summarising the processing algorithm.

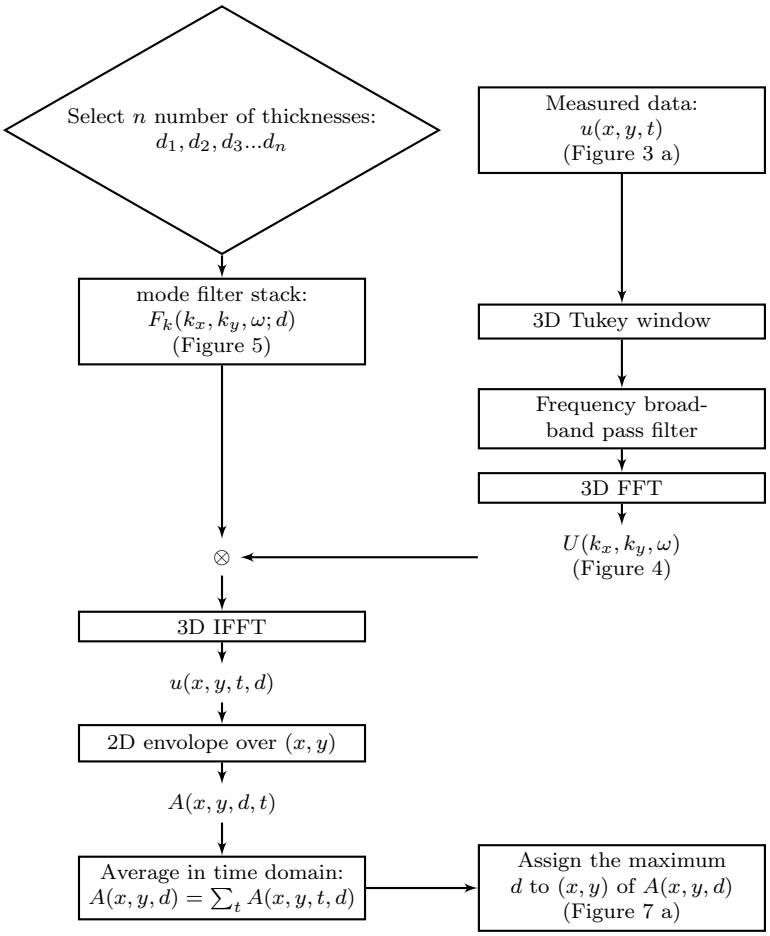

Figure 1: Thickness correlation

2.2. Dispersion calculation

Lamb waves are dispersive, that is to say their velocity changes with their frequency thickness product [22]. The relation between frequency, thickness and wavenumber are described by the Rayleigh-Lamb Equations [22]. The relation for symmetric and anti-symmetric modes are given in Equation1 and Equation 2 respectively, where h denotes the half plate thickness, d.

$$\frac{\tan(qh)}{\tan(ph)} = \frac{-4k^2pq}{(q^2-k^2)^2} \tag{1}$$

$$\frac{\tan(qh)}{\tan(ph)} = \frac{(q^2-k^2)^2}{4k^2pq} \tag{2}$$

The values of p and q are given by Equations 3 and 4 respectively [22] where k denotes the angular wavenumber. As such $k = 2\pi\tilde{\nu}$. ω denotes the angular

frequency so that $\omega = 2\pi f$. c_l and c_t denote the longitudinal and transverse speed of sound in the material respectively.

$$p^2 = \left(\frac{\omega}{C_l}\right) - k^2 \tag{3}$$

$$q^2 = \left(\frac{\omega}{C_t}\right) - k^2 \tag{4}$$

The dispersion curves in terms of frequency thickness product and wavenumber can be calculated using a bisection method. Further information on solving the Rayleigh-Lamb Equations can be found in [22]. Figure 2, shows dispersion curves calculated for the fundamental modes of both S_0 and A_0 waves in a 3mm thick aluminium plate. For rolled aluminium $c_l = 6420ms^-1$ and $c_t = 3040ms^-1$ were used [23].

The A_0 mode is used as its out of plane motion gives a better signal to noise ratio as well as its dispersive nature means that a greater change in wavenumber would be expected for a given thickness change at the frequency thickness product ranges used in this work compared with the S_0 mode.

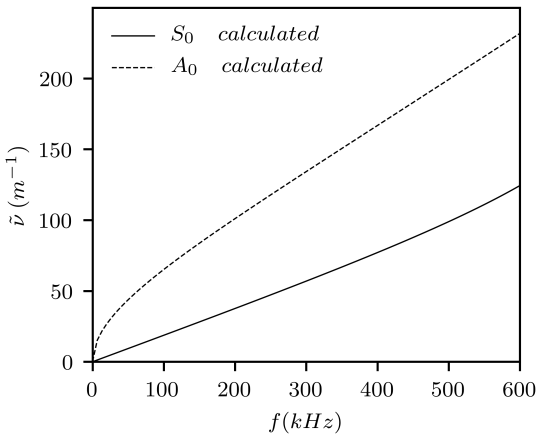

Figure 2: S_0 and A_0 dispersion curves for 3mm thick aluminium plate.

2.3. Frequency-wavenumber domain data

The full field wave velocity data that is captured can be stored in the form of a 3D matrix, $u(x, y, t)$, with two spatial domain axes, x and y, and one temporal domain axis, t. The driving sensor was placed at $X = 312.5mm$ and $Y = -12.5mm$ with respect to the axes given in Figure 3. A snapshot in time of the example data is shown in Figure 3 (a) while Figure 3(b) shows a thickness map of the true thickness of Phantom plate 1.

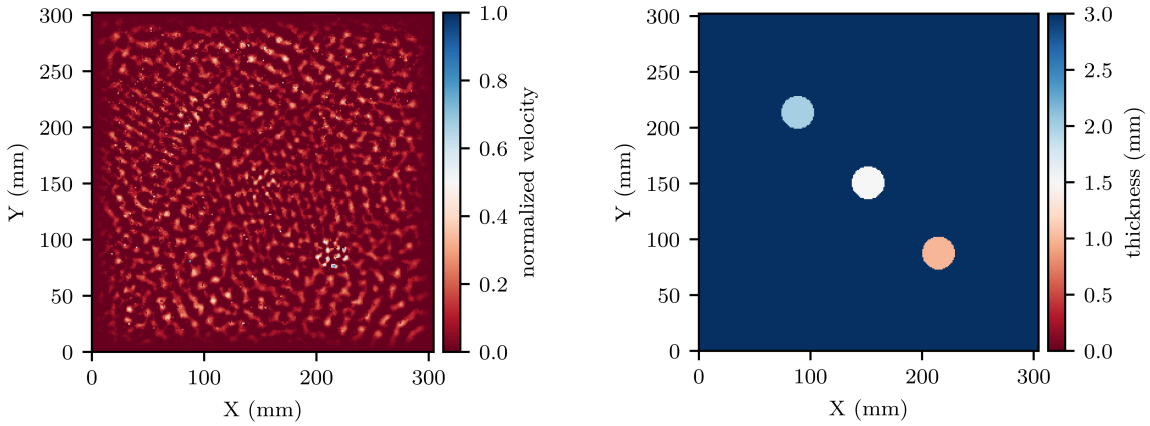

(a) (b)

Figure 3: Phantom 1 (a) wave-field response at time t (b) True thickness map

In order to convert the wave-field data to the frequency domain, $U(k_x, k_y, \omega)$, it is windowed using a 3D Tukey window. This is a 3D extension of the one dimensional Tukey window, w_n as given by Equation 5.

$$w(n) = \begin{cases} 1, & 0 \leq |n| \leq \alpha\dfrac{N}{2} \\ 0.5\left[1 + \cos\left[\pi\dfrac{n - \alpha\frac{N}{2}}{2(1-\alpha)\frac{N}{2}}\right]\right], & \alpha\dfrac{N}{2} \leq |n| \leq \dfrac{N}{2} \end{cases} \tag{5}$$

As α varies form zero to unity the window, of length N, varies from a rectangular window to a cosine window. A Tukey (also known as tapered cosine) window [24] was chosen for its ability to smooth to zero at the edges while minimising the amount of information lost [24]. After windowing, the data is zero buffered spatially to the nearest power of two and a 3D fast Fourier transform, Equation 6 is applied, converting each axis of the data into its corresponding frequency domain.

$$U(k_x, k_y, \omega) = \mathcal{F}_{3d}(u(x, y, t)) \tag{6}$$

While in the frequency domain a broadband bandpass temporal frequency filter may be applied with cut off frequencies selected based on the excitation method and excitation frequency. Generally the pass band will be larger then the excitation frequency range and only be used to remove environmental noise rather then separating different frequency responses. A 3^{rd} order Butterworth bandpass filter is used as it has a very flat frequency response in the pass band [25] and any inaccuracies in cut-in and cut-off frequencies are not of great concern.

2.4. Lamb wave mode filter design

Using the equations described in Section 2.2 the expected wavenumber for a given frequency and mode can be found. Figure 4 shows full field data from phantom 1 sliced in a temporal (a) and spatial (b) frequency axes. On each figure values are also plotted that have been calculated using the Rayleigh-Lamb equations described in Section 2.2.

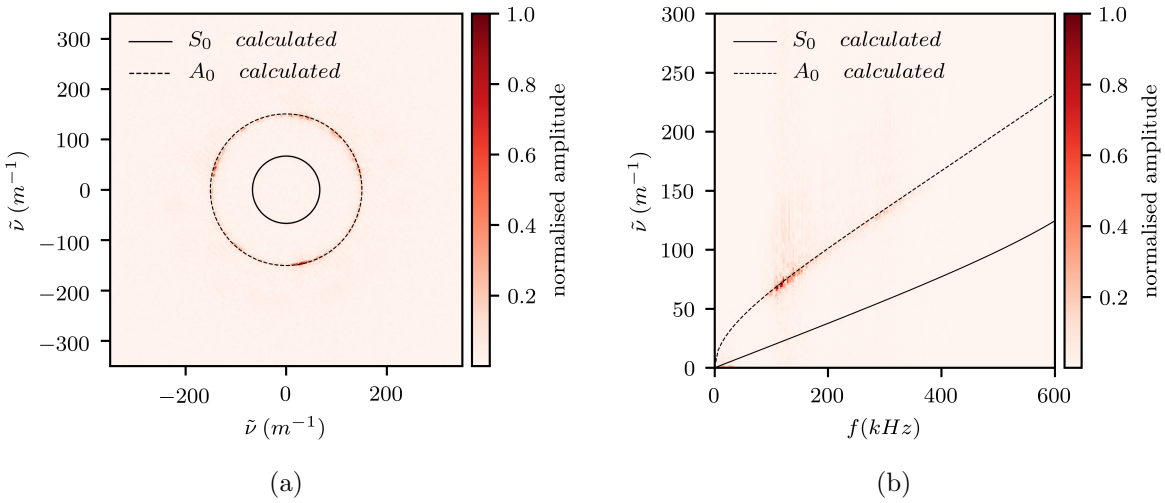

Figure 4: Freqency domain data $U(k_x, k_y, t)$ sliced at (a) $f = 200kHz$ and (b) $k_y = 0$ and Rayleigh-Lamb equation solutions.

Both Figure 4 (a) and (b) show a band of energy around the calculated values of the A_0 mode. A filter can be built around this distinct band of energy. To ensure symmetry in the wavenumber domain the filter is calculated as a stack of 2D filters at each frequency slice ω in the wavenumber-wavenumber domain.

To create the filter, a two dimensional circular projection of a bandpass filter, $T(n)$ is placed in a 2D filter matrix $F_k(x, y)$ as given by Equation 7. x and y range from $-p_x/2$ to $p_x/2$ and $-p_y/2$ to $p_y/2$ where p_y and p_x are the number of sample points in the x and y direction respectively.

$$F_k(x, y) = T(n) \tag{7}$$

Where n is given by Equation 8.

$$n = \sqrt{(x)^2 + (y)^2} \tag{8}$$

For a filter function, $w(n)$, with a bandpass width of k_{width} and a pass band centred around k_{pass} a 2D bandpass filter, $T(n)$, can be calculated using Equation 9, allowing a wavenumber filter, $F_k(k_x, k_y, \omega)$, can be calculated.

$$T(n) = \begin{cases} 0, & 0 \leq |n| \leq k_{pass} - \dfrac{k_{width}}{2} \\ w(n), & k_{pass} - \dfrac{k_{width}}{2} \leq |n| \leq k_{pass} + \dfrac{k_{width}}{2} \\ 0 & k_{pass} + \dfrac{k_{width}}{2} > |n| \end{cases} \tag{9}$$

The shape of the filter as well as its bandpass width affects the accuracy of the results. For similar image filtering problems a Gaussian filter is a common choice. This has also been used by Flynn et al. in a similar context [13, 26].

The full mode filter is created using the steps given below for a given mode, thickness and material:

1. Select frequency value, ω_0, of first frequency bin ω_{bin} in $U(k_x, k_y, \omega)$
2. Using the Rayleigh-Lamb Equations calculate the wavenumber value, k, for the selected mode and thickness, d at ω_0
3. Create a 2D window, $F_k(x, y)$, with a centre value of k, as described by Equation 14
4. Move onto next frequency bin and repeat steps 1-3 and stack the 2D filter slices created to create a matrix, $F_k(k_x, k_y, \omega; d)$

Figure 5 (a) shows a slice of a filter created for the example data centred around 2.9mm in the wavenumber domain. Figure 5 (b) shows the same filter sliced in the wavenumber-frequency domain along with calculated A_0 and S_0 dispersion curves. The filter has a bandwidth of $\tilde{\nu} = 120m^{-1}$ and is the shape of a flat top filter window.

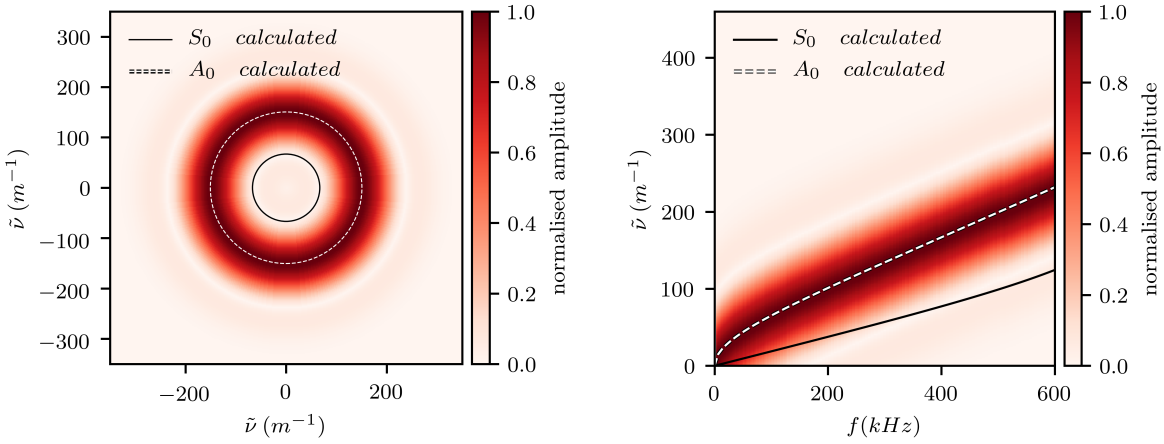

Figure 5: Freqency wavenumber filter, $U(k_x, k_y, t)$, sliced at (a) $f = 450kHz$ and (b) $k_y = 0$ and Rayleigh-Lamb equation solutions.

It is now possible to create a filter bank, $F_k(k_x, k_y, \omega; d)$ of mode filters calculated about different thicknesses d where $d = [d_1, d_2, d3...d_n]$. The dispersive nature of Lamb waves means that for a frequency the relationship between plate thickness and wave number change is non-linear. The thicknesses, d, of a filter bank should be chosen so that a maximum overlap between filters in the wavenumber domain is not exceeded. Figure 6 shows the relation between wavenumber and thickness at a given frequency. This also demonstrates the reduction in thickness resolution at increasing thickness.

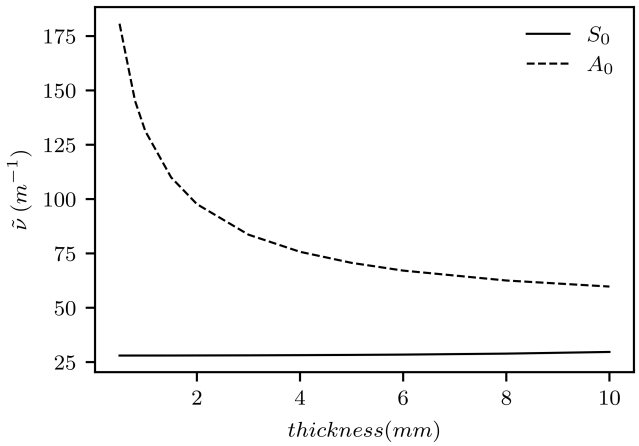

Figure 6: Thickness against wavenumber at $200kHz$

2.5. Monogenic signal analysis

Once a wave-field has been filtered by the filter bank in the frequency-wavenumber domain an Inverse Fast Fourier Transform (IFFT) can be used to return the data to the temporal and spatial domain. The average amplitude of the filtered wave-field at each time interval gives a measure of the amount of energy remaining after each filter has been applied.

In a one dimensional problem this would simply be done by using the Hilbert transform with which the complex analytic signal can be found and the envelope of a signal calculated. The Riesz transform is an extension of this same principle to higher dimensions [27]. The monogenic signal being the higher dimensional equivalent of the analytic signal. The monogenic signal is applied spatially at each temporal sample to give the instantaneous local energy as used by Langley et al. [28] and Flynn et al. [26].

The Riesz transform of a real 2D signal, $u(x, y)$, will have three components as shown in Equation 10, 11 and 12 [28] .

$$L_{ox}(k_x, k_y) = j\frac{k_x}{\sqrt{k_x^2 + k_y^2}}U(k_x, k_y) \tag{10}$$

$$L_{oy}(k_x, k_y) = j\frac{k_y}{\sqrt{k_x^2 + k_y^2}}U(k_x, k_y) \tag{11}$$

$$L(k_x, k_y) = U(k_x, k_y) \tag{12}$$

The amplitude of the 2D signal can then be found using Equation 13 where $l(x, y)$ is the inverse Fourier transform of $L(k_x, k_y)$.

$$A(x, y) = \sqrt{I(k_x, k_y)^2 + I_{ox}(k_x, k_y)^2 + I_{oy}(k_x, k_y)^2} \tag{13}$$

As with a 1D signal a large variety of scale in the signal causes inaccurate results. Multi-frequency excitation means there are multiple wave lengths present but even at relatively large frequency ranges the range in wavelength is small enough to consider the signal as band limited.

2.6. Mode filter application

Once the filter bank, $F_k(k_x, k_y, \omega; d)$, has been calculated each filter at thickness d can be multiplied with the measurement matrix, $U(k_x, k_y, \omega)$ in the frequency domain, before being returned to the temporal spatial domain with an inverse 3D Fourier transform, $\mathcal{F}_{3D}^{-1}$, as in Equation 14.

$$u(x, y, t; d) = \mathcal{F}_{3d}^{-1}[F_k(k_x, k_y, \omega; d)U(k_x, k_y, \omega)] \tag{14}$$

The local energy of each filtered response at thickness d can then be calculated using Equation 13 at each time step giving $A(x, y, t, d)$. This can then be averaged in the time domain using Equation 15.

$$A(x, y, d) = \sum_t A(x, y, t, d) \tag{15}$$

The filter thickness d_n, of the filter which maximises the energy at sample point (x, y) is then assigned to that point creating a thickness map $d(x, y)$ as given by Equation 16. The thickness map calculated for Phantom 1 is shown in Figure 7(a) and the error which is given by subtracting true thickness from the measured results are shown in Figure 7(b). A low thickness error is shown across the specimen with higher error around the edges of the thickness changes. This is due to the limited spatial sampling frequency, with over 1mm between spatial sample points as well as the wavelength of the driven frequencies ranging from approximately $17mm$ to $6mm$. Furthermore, this will result in a small region where a change in wavelength cannot be identified.

$$d(x, y) = \max_d A(x, y, d) \tag{16}$$

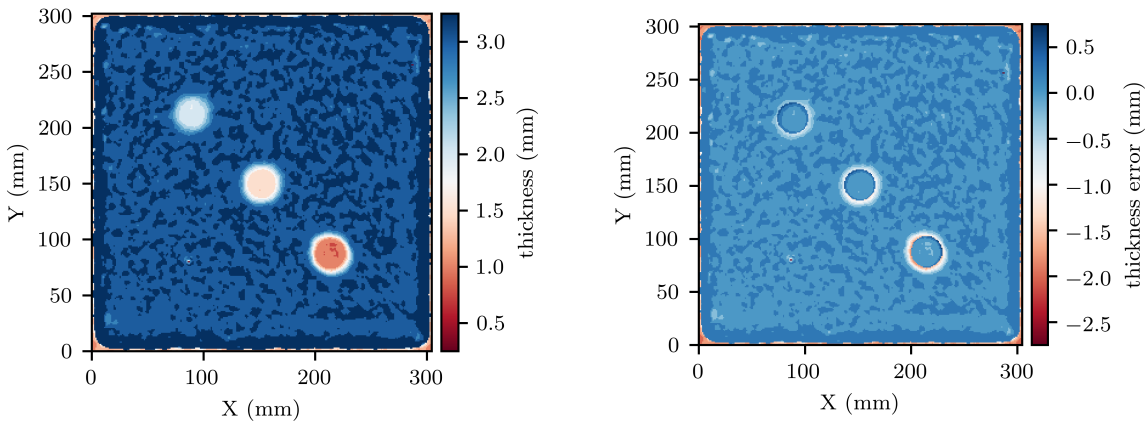

(a) (b)

Figure 7: Phantom 1 (a) Phantom 1 resulting thickness map (b) thickness error

2.7. Mode filter width investigation

In previous papers that use wavenumber domain filtering, Gaussian filters were used at a single bandwidth [13, 26]. This is a common choice in similar image processing applications. Work by Felsburg et al. [29] shows the importance of filter shape selection when applying a scale space before calculating the monogenic signal. To further investigate the selection of filter bandwidth and filter shape for the application proposed an ideal thickness map, $I(x, y)$, was calculated with the same dimensions and sampling frequency as the measured thickness map. By subtracting a calculated thickness map from the ideal map a mean percentage error (MPE) can be found.

Using Equation 17 the MPE was calculated for each matrix of results, $d(x, y)$, where n is the number of spatial sampling points.

$$MPE = \frac{100}{n} * \sum_{t=1}^{n} \frac{I(x, y) - d(x, y)}{I(x, y)} \tag{17}$$

2.8. Experimental setup

All measurements were completed using a 3D SLDV. The full field data was captured using the Polytec PSV-500-3D-M in conjunction with an external camera. Data was exported from Polytec's proprietary software containing three dimensional spatial coordinates of each sample point as well as the velocity in three dimensions for that point. An area of 350mm by 300mm was measured with 285 and 239 samples in each direction respectively. 50 measurements were

averaged at each sample point. A temporal sampling frequency of 2.56 MHz with a sample length of 0.0004 seconds was used. Once data was acquired it was processed using a developed Python script. To ensure even spatial sampling, the wave field at each time sample was interpolated in 2D using spatial coordinates as given by the 3D SLDV and re-sampled over an evenly spaced grid in the spatial domain of the same number of points measured. Interpolation was done using a cubic spline, a smoothing factor of 0 and a surface interpolation algorithm as described by Dierckx [30]. While 3D velocity data was gathered for this work only out-of-plane velocity was considered. A 1D LDV would have sufficed for this work however, the use of a 3D system will help allow this technique to be expanded to 3D structures in the future. Both a Vallen System VS900-M PZT sensor with a face diameter of 20mm and a Pancom PicoZ PZT sensor with a face diameter of 5mm were used to excite the phantom plate. While transient excitation can offer clear wave-field images the time taken to acquire data is significantly larger then that taken to acquire data from steady state excitation. With transient excitation, time has to be allowed between each measurement for the signal to ring down in the plate before the next excitation. Steady state excitation also allows for better signal to noise ratios as energy is continually driven into the plate. Signal to noise ratio is further improved in smaller plates as waves will be reflected off all edges and thickness change features. While this adds complication to the nature of the wave-field it is a desirable feature as the multiple propagation directions add more information in the wavenumber-wavenumber domain to which each mode is filtered, reducing error. This effect could be further enhanced by using multiple sensors on a single structure being driven simultaneously. This lack of ring down also makes sensor position less critical for materials with lower acoustic attenuation such as aluminium. In larger structures with fewer reflective surfaces or materials such as composites with higher attenuation, increased damping as distance from the driving sensor is increased, is likely to affect measurements. This effect could also be mitigated by using multiple driving sensors. In this investigation, all measurements were completed using steady state excitation. The plate was excited using a continuous 200Vpp sine wave signal driven at 75 kHz, 150 kHz, 300 kHz and 400 kHz with the larger Vallen sensor. For multi-frequency excitation a sine wave signal was Frequency Modulated (FM) upwards between 75 kHz and 400 kHz at a rate of 2.45 kHz. The FM signal was generated using both Vallen sensors individually and was windowed using a Tukey window allowing the signal to be continually repeated without transient spikes between repetitions. All signals were generated using a Red Pitaya STEMLab 125-14 board in conjunction with a Krohn-Hite 7500 amplifier. The measurements were filtered using a Gaussian shaped mode filter with a standard deviation value of 15 applied to the Gaussian kernel and a bandpass width of $\tilde{\nu} = 100m^{-1}$. The thickness to which the mode filters were calculated were chosen so that they would have a minimum separation of 0.1mm or a minimum separation of $\tilde{\nu} = 3m^{-1}$, whichever was smaller. A value of $\tilde{\nu} = 3m^{-1}$ was chosen as this was approximately the width of each frequency bin in the wavenumber domain. This gives a large overlap between filters leading to an over-complete interpretation which helped give consistent

and repeatable results. Values of transverse, c_t and longitudinal, c_l, speed of sound for aluminum were taken to be $3040ms^{-1}$ and $6420ms^{-1}$ respectively [23]. A schematic of the experimental set up is shown in Figure 8.

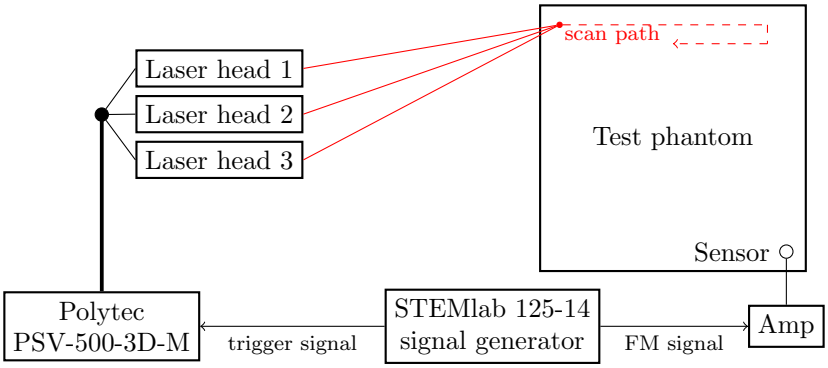

Figure 8: Experimental setup

2.9. Test specimens

To validate the abilities of this algorithm a second plate, Phantom 2 was created. Phantom 2 consisted of a flat 400mm x 400mm, 8mm thick 6082 T6 aluminium plate with a 1mm stepped and a ramped thickness change from 1mm to 8mm. Circular thickness changes were also present at every second 1mm thickness change and were mirrored on the thickness ramp. These were 30mm, 17.5mm, 10mm and 4mm in diameter. The 1mm thick area of the plate had thickness reductions from 1mm to 0.9mm and 0.5mm. Over the rest of the plate thickness reductions were from 3mm to 2mm, 5mm to 3mm and from 7mm to 4mm. This allows spatial and depth resolution to be tested over a large range of thicknesses. A thickness map of Phantom 2 is given in Figure 9. The sensors were coupled with grease and placed at $X = 175mm$ and $Y = 350mm$ in relation to the axes in Figure 9. It was calculated using the same spatial sampling frequency as the measurement leading to a quantisation representation of an ideal test result.

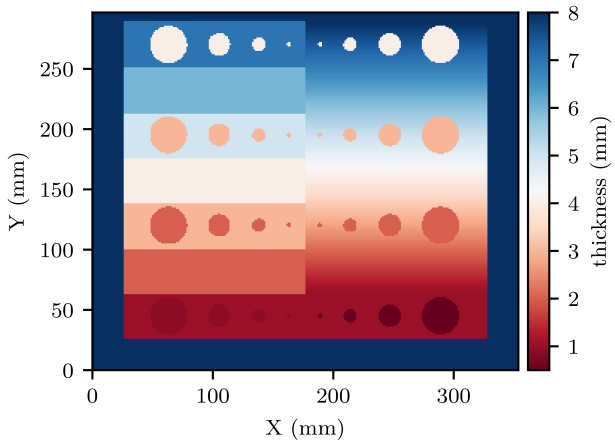

Figure 9: Phantom 2 plate thickness map

3. Results and discussion

Resulting single frequency thickness maps are shown in Figure 10. These excitations were single frequency, but the steady state nature of the excitation and interactions of the waves with plate features a broader range of frequencies are present in the plate. A full mode filter was applied over the entire frequency range which results in a greater data density than a single frequency slice being passed through a simple wavenumber filter bank, as done in previous work [12, 13, 26, 31].

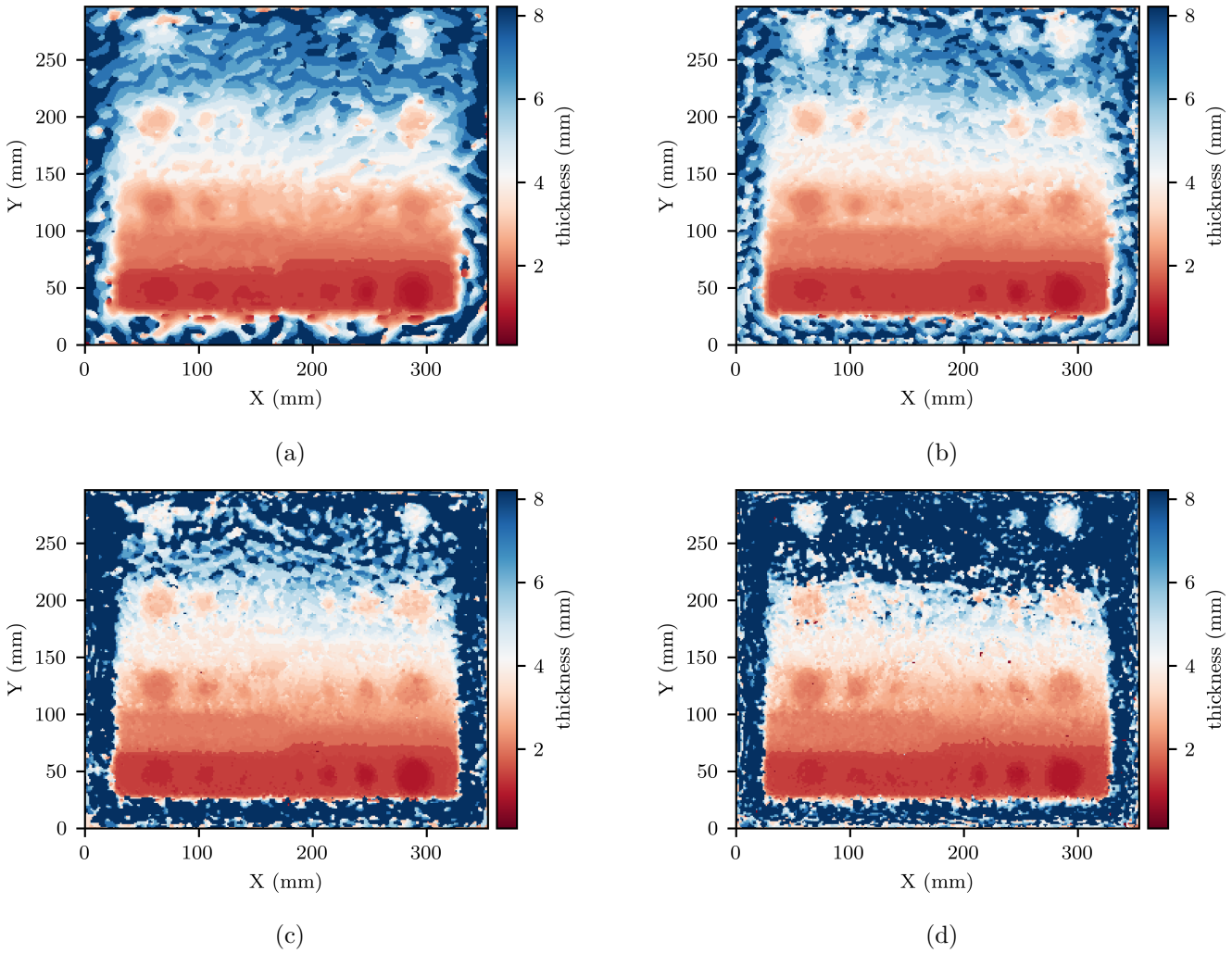

Figure 10: Single frequency Vallen sensor excitation (a) 75 kHz (b) 150 kHz (c) 300 kHz (d) 400 kHz

In Figure 11 the resulting thickness maps are shown for FM excitation. The plate was separately excited using the Vallen and PicoZ sensors with the results shown in Figure 11 (a) and (b) respectively. While the Vallen sensor is able to generate much larger amplitude, and therefore much better signal to noise ratios, the results are very similar. The PicoZ and Vallen sensors also have different resonances resulting in different frequencies being excited to different levels in the structure. Despite the differences in excitation the comparative nature of the filtering technique gives remarkably consistent results.

The 1mm to 3mm thick areas of the phantom are generally well resolved in

all single frequency results shown in Figure 11. Thickness changes of 0.5mm at 1mm are visible down to a diameter of 10mm. At the higher frequencies of 300 kHz and 400 kHz the 4mm diameter thickness change is also visible. At the spatial sampling frequency, 4mm represents about three samples (or pixels). The 0.1mm thickness change at 1mm plate thickness is not well resolved with some being visible at higher frequencies but without clear edges. FM excitation results show greater feature clarity across the plate with a smoother thickness map giving a better representation of true thickness with substantially less noise in the thickness estimates. The multi-frequency excitation means there is more information present in the frequency-wavenumber domain. As an example with the temporal sampling frequencies used here the FM excitation covered over 130 frequency slices in the frequency domain, compared with 10 to 20 frequency slices excited by single frequency excitation. This allows even single frequency excitation to make use of mode filtering over simple wavenumber filtering. The same spread of frequency could lead to inaccuracies when using simple wavenumber filtering as more then one wavelength is present for a given thickness over a frequency range. This greater quantity of information that is able to be gathered is likely one of the reasons edges and features are resolved with less noise in the FM results.

At a thickness larger than 4mm clarity becomes limited and the 30mm diameter thickness changes become distorted and difficult to identify at 7mm plate thickness in all single frequency excitations. The results shown in Figure 11 on the other hand show good clarity down to a defect size of 17.5mm diameter even at a thickness of 7mm. The noise in thickness measurements present in single frequency results is on a scale of the wavelength of the excitation frequency. While at low frequency larger thicknesses are better resolved, as in Figure 10 (a), at the highest frequency of 400 kHz the maximum thickness value is assigned to most points thicker then 5mm.

In Figure 11 the noise is at very low levels with consistent thickness readings across areas of uniform thickness. At thicknesses larger then 6mm the depth resolution drops off and the thickness map begins to lose accuracy. It is important to note that at the larger thickness of 7mm a wavenumber change of $\tilde{\nu} = 3m^{-1}$ corresponds to a thickness change of over a millimeter leading to quantisation in the thicknesses.

Despite the same frequencies being covered with single frequency excitation none of the FM results are able to give the same accuracy at the the larger thicknesses. This shows that it is not simply a matter of the excitation frequency being appropriate for a given thickness but that mode based filtering is able to exclude information that does not conform to the behaviour of the A_0 Lamb mode in the wavenumber-frequency domain and therefore gives a better measure of the likely thickness. Using FM excitation requires little prior knowledge of the part being inspected as excitation frequencies do not have to be chosen for a particular thickness range. While FM excitation out-performed single frequency excitation it is important to note that FM excitation spreads energy over a large frequency range leading to a trade-off between signal-to-noise ratio and the bandwidth of the FM excitation. It is noted that the edges of the plate

suffer from edge effects due to the windowing approach. If completing larger scans this would simply require a small overlap between scan areas to resolve.

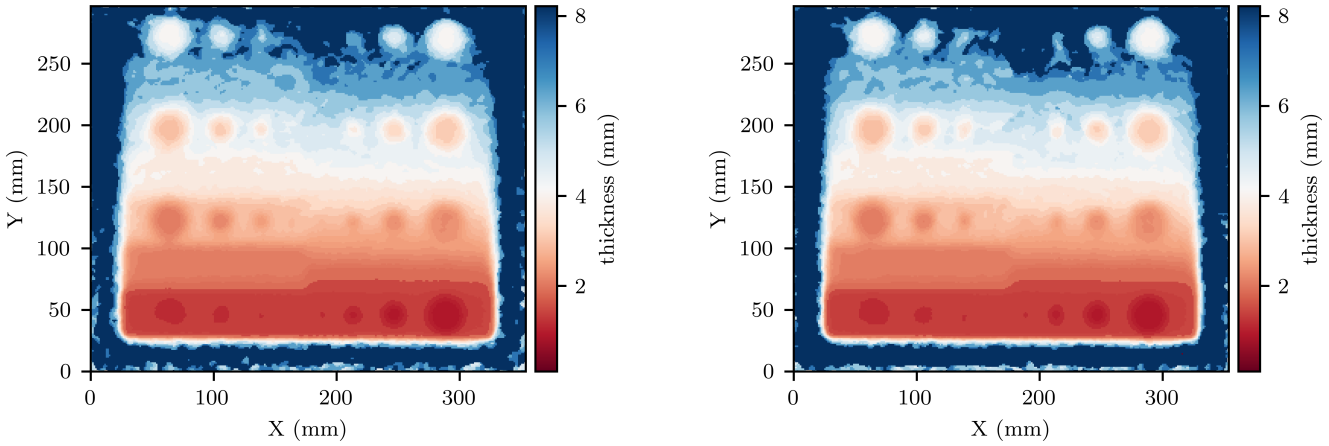

Figure 11: 75kHz to 400kHz FM excitation signal (a) Vallen sensor (b) PicoZ sensor

Figure 12 shows thickness for slices in the Y direction of Phantom 2 at X=200mm along the ramp. Thickness is overestimated across all thickness maps with the 1mm thick area being estimated at 1.34mm. As shown in Figure 12 this error reduces as thickness increases but the tendency to overestimate remains. This is likely due to inaccuracies in transverse and longitudinal speed of sound values used to calculate dispersion curves as well as as the assumptions made when using the Rayleigh-Lamb equations used to predict dispersion relations.

The lower frequencies shown in Figure 12 (a) match the FM results closely until around the 4mm thickness at which point the thickness of the single frequency excitation results begin to lose accuracy. At thicknesses greater then 5mm the FM excitation begins to out-perform the single frequency excitation significantly with large spikes and dips in thickness estimates in single frequency measurements. The higher frequency single frequency excitations shown in Figure 12 (b) match actual thickness well until 3mm. At thicknesses larger than 5mm the thickness estimate of the high frequency single frequency excitation begins to break down. 400 kHz for example gives estimates ranging from below 4mm to over 8mm in a very small area of 6mm thickness.

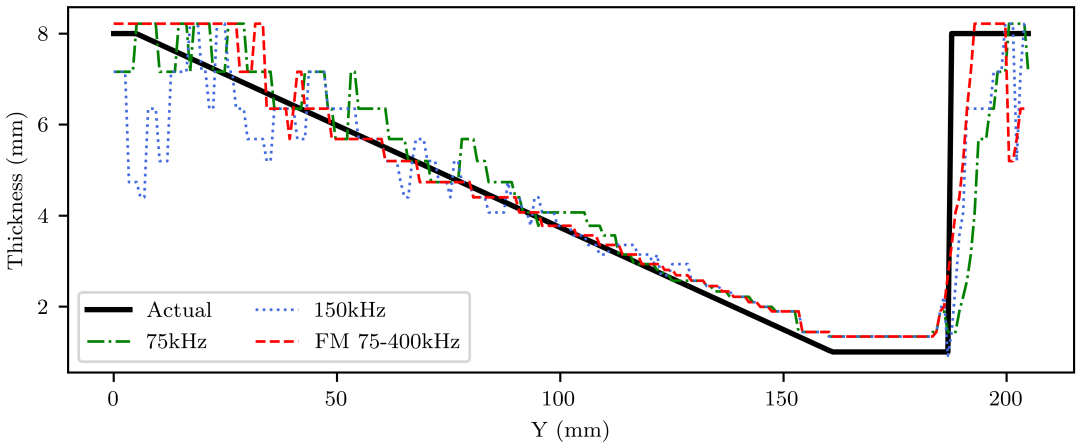

(a)

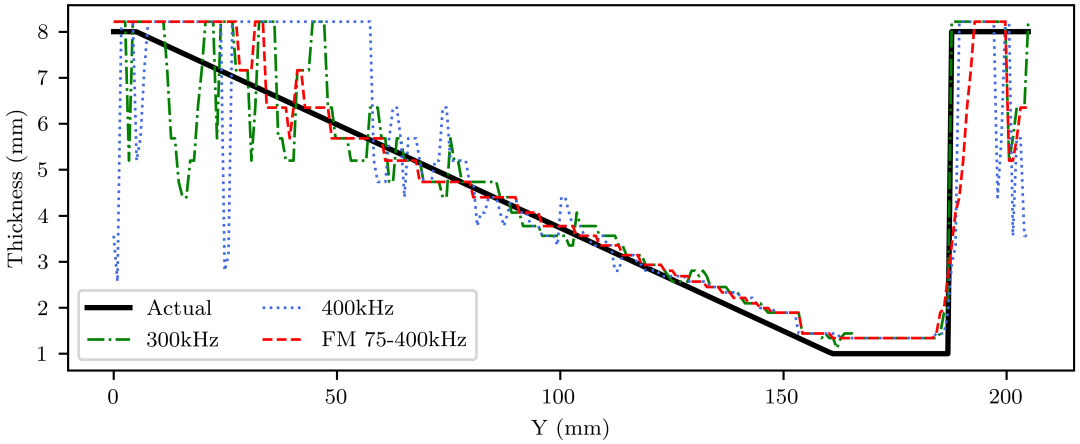

(b)

Figure 12: Horizontal slice at X=200mm (a) low frequencies (b) high frequencies

Filter width and shape were chosen after the calculation of results using a Gaussian filter with a standard deviation of 15 applied to the filter kernel and a Flat top filter over a range of widths from $\tilde{\nu} = 40m^{-1}$ to $\tilde{\nu} = 500m^{-1}$. Figure 13 shows the MPE as given by Equation 17 over a range of bandpass widths and filter shapes.

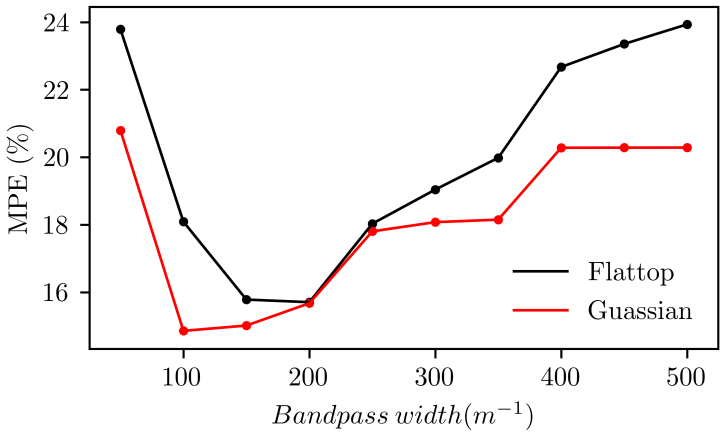

Figure 13: MPE with different window sizes and shapes

The Lowest MPE of 14.86% is given by a Gaussian filter with a bandpass width of $\tilde{\nu} = 100m^{-1}$. While this filter gives the lowest mean percentage error it is not necessarily the best filter for resolving all the thicknesses present on the Phantom 2 plate as percentage error of thin areas of the plate will have a larger effect on the MPE.

MPE was also calculated for all four steady state excitations as well as the FM excitation and is shown in Table 1. The values are calculated for the area of the plate were Y is larger then 150mm, the thick half of the plate, and the lower half where Y is less then 150mm, containing the thinner areas of the plate. Both area classifications still contain the 8mm thick border.

Table 1: MPE at different areas

Excitation	Sensor	Area	MPE
75kHz	Vallen	all	19.93%
150kHz	Vallen	all	18.68%
300kHz	Vallen	all	18.25%
400kHz	Vallen	all	20.21%
75kHz - 400kHz	Vallen	all	14.86%
75kHz - 400kHz	PicoZ	all	14.79%
75kHz	Vallen	$Y > 150$mm	12.94%
150kHz	Vallen	$Y > 150$mm	12.42%
300kHz	Vallen	$Y > 150$mm	14.36 %
400kHz	Vallen	$Y > 150$mm	18.09%
75kHz - 400kHz	Vallen	$Y > 150$mm	8.32%
75kHz - 400kHz	PicoZ	$Y > 150$mm	8.71 %
75kHz	Vallen	$Y < 150$mm	26.66 %
150kHz	Vallen	$Y < 150$mm	25.50%
300kHz	Vallen	$Y < 150$mm	24.30 %
400kHz	Vallen	$Y < 150$mm	23.68%
75kHz - 400kHz	Vallen	$Y < 150$mm	23.38%
75kHz - 400kHz	PicoZ	$Y < 150$mm	22.94 %

When considering the entire plate FM excitation out-performers all single frequency excitation with the 300 kHz single frequency excitation showing the best results of single frequency excitation. When examining the thicker area of the plate the FM excitation greatly out-performs any of the single frequency excitations. The 300 kHz single frequency excitation does however match FM excitation when only examining the thinner areas of the plate. The smaller thickness also means that any error due to quantisation will result in a larger percentage error. While MPE gives a measure of error it does not paint a complete picture of the clarity of the results. When looking at the resulting thickness maps shown in Figure 10 and 11 it is clear that the FM excitation offers clearer results with more defined features that closely match the ideal thickness map. With out prior knowledge of a part or for parts spanning multiple thickness ranges the advantage of FM excitation in combination with mode filtering is clear.

4. Conclusion

A method of calculating mode based filters and applying them to wave-field data generated with FM excitation was proposed. Mode filtering to gain thickness maps was performed on two phantom plates with a large thickness range from 0.5mm to 8mm with single and FM excitation. Single frequency excitation was able to identify defects at low thicknesses but unable to cover the broad thickness range presented. Clarity of features and edges was further increased by using FM excitation along with mode filtering. Multi frequency data gained from a frequency modulated excitation gave a thickness map with lower noise and ability to identify defects across the whole thickness range with a single laser

vibometer measurement. The importance of filter bandpass size and shape was shown. While this work was completed on isotropic materials the primary aim is to expand the technique to non-isotropic composite materials in the future. While theoretical methods of solving dispersion curves are available for composites their lack of accuracy the and detailed knowledge of layup required create further challenges to this expansion. While only demonstrated on a flat plate the use of a 3D scanning laser vibometer was successfully shown giving the ability to also further this technique to more complex part geometries.

5. Acknowledgements

We would like the thank the EPSRC doctoral program for providing funding for this work. We would also like to thank Paul Leach for machining both phantom plates used in this work and Karin Purcell for helping proof read this work.

[1] Remzi Saltoglu, Nazmia Humaira, and Gokhan Inalhan. Scheduled Maintenance and Downtime Cost in Aircraft Maintenance Management. *Engineering and Technology International Journal of Aerospace and Mechanical Engineering*, 10(3):602–607, 2016.

[2] Vladimir P. Vavilov and Douglas D. Burleigh. Review of pulsed thermal NDT: Physical principles, theory and data processing. *NDT and E International*, 73:28–52, 2015.

[3] Sandeep Kumar Dwivedi, Manish Vishwakarma, and Prof Akhilesh Soni. Advances and Researches on Non Destructive Testing: A Review. *Materials Today: Proceedings*, 5(2):3690–3698, 2018.

[4] Jens Baaran. Study on visual inspection of composite structures. Technical report, Institute of Composite Structures and Adaptive Systems, Braunschweig, 2009.

[5] Yuanqiang Ren, Lei Qiu, Shenfang Yuan, and Zhongqing Su. A diagnostic imaging approach for online characterization of multi-impact in aircraft composite structures based on a scanning spatial-wavenumber filter of guided wave. *Mechanical Systems and Signal Processing*, 90:44–63, 2017.

[6] Lei Qiu, Bin Liu, Shenfang Yuan, and Zhongqing Su. Impact imaging of aircraft composite structure based on a model-independent spatial-wavenumber filter. *Ultrasonics*, 64:10–24, 2016.

[7] Yun Kyu An, Zhiqi Shen, and Zhishen Wu. Stripe-PZT sensor-based baseline-free crack diagnosis in a structure with awelded stiffener. *Sensors (Switzerland)*, 16(9), 2016.

[8] A. S. Purekar and D. J. Pines. Damage detection in thin composite laminates using piezoelectric phased sensor arrays and guided lamb wave interrogation. *Journal of Intelligent Material Systems and Structures*, 21(10):995–1010, 2010.

[9] Peter D. Juarez and Cara A C Leckey. Multi-frequency local wavenumber analysis and ply correlation of delamination damage. *Ultrasonics*, 62:56–65, 2015.

[10] Eric B Flynn. Embedded Multi-Tone Ultrasonic Excitation and Continuous-Scanning Laser Doppler Vibrometry for Rapid and Remote Imaging of Structural Defects. *7th European Workshop on Structural Health Monitoring*, pages 1561–1567, 2014.

[11] Eric B. Flynn, Jr Lee, Gj Jarmer, and G Park. Frequency-wavenumber processing of laser-excited guided waves for imaging structural features and defects. *6th European Workshop on Structural Health Monitoring*, pages 1–8, 2012.

[12] Jun Young Jeon, Sehyeok Gang, Gyuhae Park, Eric Flynn, To Kang, and Soon Woo. Damage detection on composite structures with standing wave excitation and wavenumber analysis. *Advanced Composite Materials*, 3046(November):1–13, 2017.

[13] Eric B. Flynn, See Yenn Chong, Gregory J. Jarmer, and Jung Ryul Lee. Structural imaging through local wavenumber estimation of guided waves. *NDT and E International*, 59:1–10, 2013.

[14] Paweł Kudela, Maciej Radzieński, and Wiesław Ostachowicz. Identification of cracks in thin-walled structures by means of wavenumber filtering. *Mechanical Systems and Signal Processing*, 50-51:456–466, 2015.

[15] O. Mesnil, C. a. Leckey, and M. Ruzzene. Instantaneous and local wavenumber estimations for damage quantification in composites. *Structural Health Monitoring*, pages 1–12, 2014.

[16] Matthew D. Rogge and Cara A C Leckey. Characterization of impact damage in composite laminates using guided wavefield imaging and local wavenumber domain analysis. *Ultrasonics*, 53(7):1217–1226, 2013.

[17] Thomas E. Michaels, Jennifer E. Michaels, and Massimo Ruzzene. Frequency-wavenumber domain analysis of guided wavefields. *Ultrasonics*, 51(4):452–466, 2011.

[18] M. Ruzzene. Frequency-wavenumber domain filtering for improved damage visualization. *AIP Conference Proceedings*, 894:1556–1563, 2007.

[19] Lingyu Yu, Cara A.C. Leckey, and Zhenhua Tian. Study on crack scattering in aluminum plates with Lamb wave frequency-wavenumber analysis. *Smart Materials and Structures*, 22(6), 2013.

[20] S.G. Pierce, B Culshaw, and Q Shan. Laser generation of ultrasound using a modulated continuous wave laser diode. *Applied Physics Letters*, 1030(December 1997):27–30, 1998.

[21] W. J. Staszewski, B. C. Lee, and R. Traynor. Fatigue crack detection in metallic structures with Lamb waves and 3D laser vibrometry. *Measurement Science and Technology*, 18(3):727–739, 2007.

[22] Joseph L. Rose. *Ultrasonic Waves in Solid Media*. The Press syndicate of the university of Cambridge, Cambridge, first edition, 1999.

[23] David R Lide. *CRC Handbook of Chemistry and Physics*. CRC Press, Boca Raton, FL,, internet v edition, 2005.

[24] F.J. Harris. On the use of windows for harmonic analysis with the discrete Fourier transform. *Proceedings of the IEEE*, 66(1):51–83, 1978.

[25] Mohit Bansal, Ritu Sharma, and Parul Grover. Performance evaluation of Butterworth Filter for Signal Denoising. *International Journal of Electronics & Communication Technology*, 1(Dec):1–5, 2010.

[26] Eric B. Flynn and Nicholas D. Stull. Toward Utilizing Full-Field Laser-Ultrasound for Practical Nondestructive Inspection with Acoustic Wavenumber Spectroscopy. In *2018 IEEE International Ultrasonics Symposium (IUS)*, pages 1–7. IEEE, oct 2018.

[27] Michael Felsberg and Gerald Sommer. The monogenic signal. *IEEE Transactions on Signal Processing*, 49(12):3136–3144, 2001.

[28] Keith Langley and Stephen J. Anderson. The Riesz transform and simultaneous representations of phase, energy and orientation in spatial vision\\. *Vision Research*, 50(17):1748–1765, 2010.

[29] Michael Felsberg and Gerald Sommer. The monogenic scale-space: A unifying approach to phase-based image processing in scale-space. *Journal of Mathematical Imaging and Vision*, 21(1):5–26, 2004.

[30] P. Dierckx. An Algorithm for Surface-Fitting with Spline Functions. *IMA Journal of Numerical Analysis*, 1(3):267–283, 1981.

[31] Elise Anne C Koskelo and Eric B. Flynn. Full-field inspection of three-dimensional structures using steady-state acoustic wavenumber spectroscopy. *AIP Conference Proceedings*, 1806, 2017.